ChemElectroChem

Articles
doi.org/10.1002/celc.202001249

**Chemistry
Europe**
European Chemical
Societies Publishing

Special Collection

Impact of Particle Size Distribution on Performance of Lithium-Ion Batteries

Lars Bläubaum,[a, c, d] Fridolin Röder,[c, d] Christine Nowak,[b, d] Hoon Seng Chan,[a, c, d] Arno Kwade,[b, d] and Ulrike Krewer*[a, c, d]

This work reveals the impact of particle size distribution of spherical graphite active material on negative electrodes in lithium-ion batteries. Basically all important performance parameters, i.e. charge/discharge characteristics, capacity, coulombic and energy efficiencies, cycling stability and C-rate capability are shown to be affected by distribution shapes. A narrow distribution with smaller particles results in better cell performance than broader and coarser distributions. However, particle size reduction has a limitation as extremely small particles show negative effect in performance. More critically,

independent of the particle size distribution, the existence of coarse particles are found to promote lithium plating, which lowers cell performance and threatens the safety of battery operation. Furthermore, impedance analysis and cycling stability show huge differences for different electrodes. Our study shows that a better understanding of the influence of particle size distribution is an important base to engineer electrodes with higher C-rate capability, higher performance, and lower safety risk due to lithium plating.

Introduction

Optimization of cell performance and safety of lithium-ion batteries (LIB) as well as the reduction of cell aging remain as core challenges in both academic research and industry development. One of the most important influencing factors is the particle size of the active materials. Particle size of active material influences the electrochemical performance of a battery.[1–3] Lithium in smaller particles has shorter solid diffusion pathways, lower overpotential, and thus, allows faster C-rate operation. At the same time, the larger surface area leads to a larger proportion of passivation layers, such as the solid electrolyte interphase (SEI), leading to an irreversible loss of capacity. Thereby, in order to optimize the electrochemical performance of batteries, it is essential to understand the effect of particle size and particle size distribution (PSD) on performance and degradation.

Active material particle production is one of the first electrode production steps. Granulation and mechanical milling are common methods to achieve a desired particle size of

active material. For silicon as anode material, ball milling delivers one of the most promising outcomes in terms of economic aspect as well as performance.[4–8] It is shown that through ball milling structures with micrometric silicon agglomerates (median size circa 10 μm) can be attained. The structure assures a shorter diffusion pathway for lithium ions, whereas the micrometric agglomerates offer a better particle network connectivity. A wide range of primary particles could arise from the ball milling process rather than just a single particle size. For battery grade graphite production, especially natural graphite, the size distribution and shape of the graphite particles is controlled by milling and classification processes.[9–11] Besides mechanical milling, there are also other techniques, for example sifting, to control particle size and PSD. Overall, it is important to consider the PSD for future optimization of cell performance and safety.

Aside from particle size and PSD, there are still many other process steps during electrode production that affect the properties of batteries. For example, calendering influences the porosity and thickness of the electrode.[12–17] The thickness of the electrode influences the diffusion pathway, because the thicker the electrode, the longer the diffusion length for ions.[15] Similar behavior applies to particle size and PSD, as they impact electrolyte diffusion pathway through tortuosity and porosity, also the solid diffusion.[18–20] High overpotential due to solid diffusion and interface resistance reduce energy efficiency and may cause safety hazards. Those aspects are particularly important at negative electrodes, where high overpotential can decrease the potential vs. Li/Li⁺ below zero volt, which can lead to lithium plating.[21] On the plated Lithium, dendrites could grow through the separator to the positive electrode, short circuiting the cells and possibly leading to thermal runaway.[22] Hence, to prevent the occurrence of lithium plating, it is important to reduce the overpotential of negative electrodes. Apart from optical ex-situ measurements, lithium plating can be

[a] L. Bläubaum, H. S. Chan, Prof. Dr.-Ing. U. Krewer
Institute for Applied Materials, Karlsruhe Institute of Technology, Adenauer-ring 20b, 76131 Karlsruhe, Germany
+49-(0)721-608-47490
+49-(0)721-608-47492
E-mail: ulrike.krewer@kit.edu
[b] C. Nowak, Prof. Dr.-Ing. A. Kwade
Institute for Particle Technology, TU Braunschweig, Volkmaroder Str. 5, 38106 Braunschweig, Germany
[c] L. Bläubaum, Prof. Dr.-Ing. F. Röder, H. S. Chan, Prof. Dr.-Ing. U. Krewer
Institute of Energy and Process Systems Engineering, TU Braunschweig, Franz-Liszt-Strasse 35, 38106 Braunschweig, Germany
[d] L. Bläubaum, Prof. Dr.-Ing. F. Röder, C. Nowak, H. S. Chan, Prof. Dr.-Ing. A. Kwade, Prof. Dr.-Ing. U. Krewer
Battery LabFactory Braunschweig, TU Braunschweig, Langer Kamp 8, 38106 Braunschweig, Germany

detected in-situ via a three-electrode system[21,23] or possibly by Nonlinear Frequency Response Analysis as suggested by Harting et al..[24]

Different active materials and particle sizes have been investigated in numerous studies. The effect of different graphite materials on the cycling stability, C-rate capability and intercalation behavior were investigated.[3,25,26] They found out that the material type, particle size, porosity, electrode thickness and loadings have an influence on the battery performance. For example, coarser particles can cause poor intercalation kinetic and slower diffusion rate. Buqa et al.[25] investigated three different graphite particle sizes (6 μm, 15 μm and 44 μm) and showed that smaller particles can achieve better capacity retention. Furthermore, Buqa et al.,[27] Goers et al.[28] and Spahr et al.[29] showed that the exfoliation, SEI formation, as well as the graphite structure are influenced by the overpotential, current density and active surface area, which are induced by different types of graphite material and particle size. During aging, Zavalis et al.[30] had proven experimentally that structural damage on positive material results in a change of particle size distribution, whereas microcracks were detected on the surface of the negative graphite materials. Besides microcracks, the negative graphite material ages mainly due to the film formation and isolation of the material, which leads to the capacity fade. Similar aging behavior that structural changes happened due to cracking has also been reported by Vetter et al..[31] Apart from graphite material, there have been several studies on other material types such as silicon, LiFePO$_4$ or LiMnPO$_4$, showing that particle size has an impact on the battery performance. In general, smaller particles improve the capacity retention as they reduce the diffusion length.[32–34] Besides from experimental studies, Mei et al.[35] and Du et al.[36] simulated the effect of particle size, in which they showed that the energy and power density increase with smaller particle size due to lower overpotential.

Few works were reported on the investigation of the impact of PSD from negative composite materials on the electrochemical performance of LIB, and a lot of them are simulation studies. Röder et al.[20] and Farkhondeh et al.[37] revealed that PSD has a large influence on cell performance. It was shown that PSD influences electrode capacity and C-rate capability. Furthermore, our modeling analysis suggested that degradation caused by changes in PSD will lead to a change in properties of the battery.[20] In detail, it was suggested that particle cracking and agglomeration cause a change in PSD, and thus, performance. Further simulation based work has been presented by Chung et al..[38] They discovered that monodisperse electrodes are able to deliver higher power density at a high discharge rate due to superior surface area to volume ratio. Moreover, the simulative work from Lee et al.[39] showed that the inhomogeneous PSD induces significant potential loss of the overall cell due to the inequality of lithium-ion concentration. Also, the model from Du et al.[36] and Taleghani et al.[40] computed the decrease of available energy with faster cycling rate, and that a coarser particle possesses higher diffusion polarisation.

Few experimental studies exists. For example, Ender et al.[41] characterized the polydispersity of graphite through 3D reconstructed X-ray tomography and concluded that the pore network of the high-energy materials is limiting the electrolyte transport. Nowak et al.[42] assessed experimentally the impact of particle size as well as PSD on a dual-ion battery system. Capone et al.[43] studied the effect of PSD for red phosphorus-carbon composite anode for sodium-ion batteries. They found out that the cycle life is impacted by different PSD of red phosphorus, where the smaller particle fraction in the range of 2 μm to 10 μm improves the cycle life. On the positive electrode, there have been several works reported that different PSD influence the battery performance, impedance behavior and processing properties.[44–46]

So far, most investigations on the impact of particle size and PSD were only conducted by simulation, probably due to difficulties in experimentally producing defined PSD at a certain mean particle size and resulting electrodes. Since these model-based studies have clearly shown that the particle size and PSD on the negative electrode in LIB has a significant impact on LIB performance and aging behavior, we think it is of high importance for improving battery performance to conduct more systematic experimental investigations. By that we can identify how PSD of negative electrodes impacts the battery performance including the aging kinetics and how PSD will change during cycling.

In this work, we will show the effect of different particle sizes and PSD using a tailored model system with spherical particles. The effects will be demonstrated at cycling, C-rate and electrochemical impedance spectroscopy (EIS) tests as well as post mortem analysis. Three different fractions from the similar batch of source material are analysed to avoid differences between the fractions regarding, for example, particle structure or surface modification. We would like to emphasize that this study is not about optimizing high cycle stability or high current capability but to investigate and understand the influence of particle size and PSD on the negative electrode properties. Therefore, we do not use conductive additives so we are able to focus the studies on the impact of the active material. We use highly spherical particles, which allows rather easy separation of different particle size and PSD. Moreover, spherical particles are usually assumed in physicochemical battery models. It will be shown that all important performance parameters, i.e. charge/discharge characteristics, capacity, coulombic and energy efficiencies, cycling stability and C-rate capability are affected by distribution shapes.

Results and Discussion

In the following, we will first analyse the impact of particle sizes and PSD on discharge capacity. On this basis, a closer investigation and discussion of the effect of particle size and PSD on the negative potential curve as well as C-rate capability is given. The performance differences between particle size and PSD are then evaluated in terms of their coulombic and energy efficiencies. Next, EIS aids in revealing the difference in dynamic behavior and kinetic contributions from different particle size and PSD.

ChemElectroChem

Articles
doi.org/10.1002/celc.202001249

Chemistry Europe
European Chemical
Societies Publishing

Discharge Capacity of the Different PSD-Electrodes

Figure 1 shows the evolution of discharge capacities and their standard deviations during cycling. At the end of the formation step, all electrodes showed similar discharge capacities at C/10, with F1 being 8% lower. However, there were differences during formation: Electrodes with coarser particles showed a faster increase of capacity during formation. Differences in discharge capacity between the electrodes become higher in C-rate and cycling tests. This behavior is expected as higher currents reveal kinetic losses such as concentration overpotentials which are strongly dependent on surface areas and diffusion lengths: The narrow medium PSD (F2) showed the highest capacity during the C-rate and cycling test with a very low standard deviation. In comparison, source material showed significantly smaller discharge capacities, even though the surface area is similar. Finally, the broad PSD with coarse particles F3 showed the poorest discharge capacity. We attribute this significant difference to the variation in poly-dispersity index (PDI) and particle size (x_{50}). Except F1, discharge capacity increases when the particle size x_{50} decreases. This experimental result confirms the simulation results by Röder et al.,[20] that narrow PSD with small mean particles induce comparably lower kinetic losses and thus, provide higher discharge capacities. However, the smallest particle size (F1) featured a better discharge capacity than the source material, but lower discharge capacity compared to F2. Therefore, the positive effect of decreasing particle size for better cell performance is limited to a certain particle size. We attribute this behavior to strongly increased SEI related losses for very small particles. This is supported by our previous studies on SEI growth[47] in which small particles lead to significantly more capacity losses due to SEI formation. A further decrease in particle size will in turn cause negative effects on the cell performance, whereby the negative effect is increasing with decreasing particle size and this can lead to strong performance losses for very small particles. In comparison to previous studies, the particle size x_{50} from F1 is less than half the size of the other small investigated x_{50} graphitic particle sizes (around 3 to 4 μm) and about 2 to 16 times smaller than commonly used x_{50} particle sizes.[25,27,42]

Besides differences in performance, the different PSD also impact degradation. Discharge capacity of F3 decreased significantly during the first 29th cycles. The same trend, but much less distinct can be observed for the source material whereas the performance of F1 and F2 remained stable. The PDI seems to be as important as the mean particle size (x_{50}) or specific volumetrical surface area (S_V). As F3 and source material showed by far large degradation. Capacity and C-rate performance improved noticeably for F3 and source material after adjusting the current of the C-rate after cycle 30 and 50 to the actual cell capacity (conducted after EIS measurement). For F3 and source material, the decrease in capacity loss between 1C and 2C rate is less prominent after cycling as compared to directly after formation, which could be due to the adjusted current load or it indicates a change in electrode properties as discussed in the following.

An overview of possible degradation mechanisms that might impact electrode properties and thus, performance is given in Figure 2. Mechanisms, which may cause capacity loss or improvement are the following: particle cracking,[30,31,48] irreversible lithium plating,[22,31] loss of active material due to macro or micro cracking that leads to contact loss and electrical isolation[1,49,50] and SEI growth.[31] One possible reason for the capacity loss of F3 could be cracking of its coarser particles, which have been similarly suggested on graphite particles by Lin et al.[51] and Bhattacharya et al..[52] Such particle cracking would increase surface area and decrease diffusion length (overpotential) as suggested by Röder et al.,[20] but contact loss by mechanical electrode degradation could also result in poor
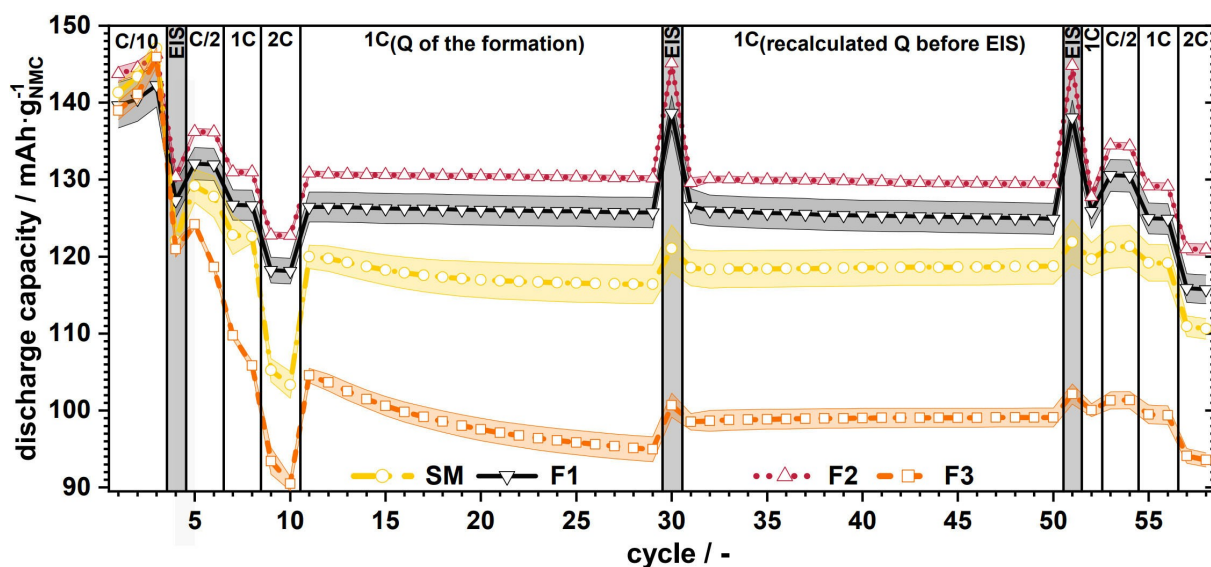
Figure 1. Specific discharge capacity vs. cycles for full cells with source material (SM) and F1 to F3 with C-rate variations; the colored range indicates the corresponding standard deviation.

ChemElectroChem

Articles
doi.org/10.1002/celc.202001249

**Chemistry
Europe**
European Chemical
Societies Publishing
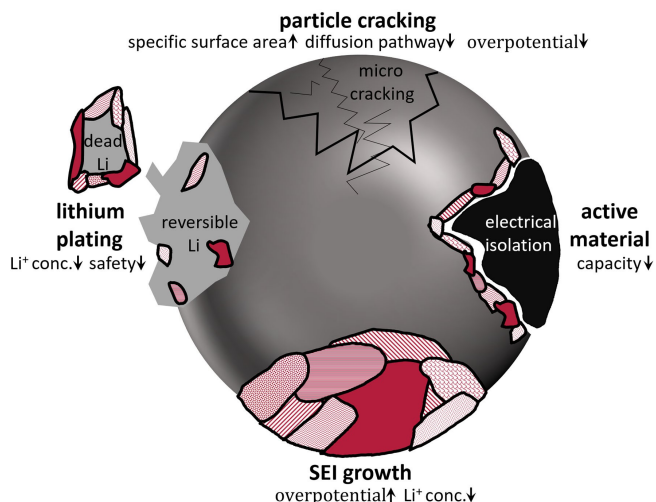
Figure 2. Illustration of possible degradation processes on negative electrode particles and their effect on properties of the battery.

Figure 3. Negative electrode potential against lithium reference vs. capacity during first charge and discharge of a lithium/graphite half cell; C/10, 25 °C, below grey line: intercalation potential range of Li^+ into graphite reported by An et al.[53]

electronic conductivity between the active materials and also disconnected to current collector. As a consequence, the capacity decreases gradually during cycling. As shown in Figure 1 the improvement of the C-rate capability after the current adjustment for F3 and source material hints that a change to higher surface area is expected. Another possible explanation is the irreversible lithium plating, also known as dead lithium, which reduces the capacity.[1,22]

Charge and Discharge Behavior

In this section, we analyse in-depth the underlying reason for the differences in capacity as a function of particle size and PSD effects from SEI growth and the intercalation potential behavior. The effects on coulomb and energy efficiencies are also analysed.

Figure 3 shows the potential of the negative electrodes for the first formation cycle. It can be seen that F3 and source material show significantly lower potentials as well as a more distinct potential drop at the beginning of charge than F2 and F1. Furthermore, F1 and F2 have more pronounced voltage plateaus between 0.25 V to 0 V, which indicates the lithium de-/intercalation stage in negative electrode materials and also the SEI formation at the early cycles.[54]

How can the different potential slopes at the beginning be explained? As the strong potential drop occurs only for F3 and source material, a thermodynamic effect can be ruled out, and kinetic effects need to be responsible for it. As shown previously, particles with smaller x_{50} particle size (F1) correspond to higher specific surface area, which then provides more active site for the undesirable side reactions such as the SEI formation.[47] This eventually results in higher irreversible loss in lithium-ions and greater passivation of the active site. On the other hand, electrodes with coarser particles, such as in source material and F3, where much stronger kinetic losses may
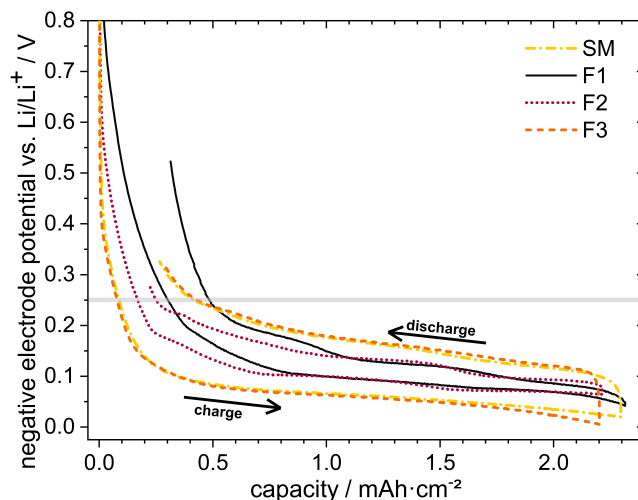
occur lead to greater voltage changes. A further indication for the larger impact of kinetic losses is the larger hysteresis during the first discharge for F3 and source material, which is small for F1 and F2. In addition, from the perspective of porosity (see Table 1), F3 and source material have higher porosity than F1 and F2. The difference of porosity between source material, F1 and F2 is smaller than source material and F3. But source material and F3 have nearly the same potential behavior. This shows that particle size and particle size distribution have a larger impact on cell performance, i.e. kinetic losses and capacity, as compared to the porosity in electrodes. It can be concluded, that for the here investigated electrodes without electric conductive additives, the transport losses through the SEI and inside the particle are more dominant than through the electrolyte.

In Figure 4, the coulombic efficiency (CE) and energy efficiency (EE) for the formation cycle are shown. They are determined according to:

$$EE = \frac{E_{discharge}}{E_{charge}} \cdot 100 \%$$

Table 1. Particle characteristics from F1 to F3 and source material; Acr: acronym, PDI: polydispersity index, S_V: specific surface area, $\varepsilon_{C,ML}$: porosity based on the coating mass loading on the electrode.

Material	Acr.	x_{10} µm	x_{50} µm	x_{90} µm	x_{98} µm	PDI $\frac{x_{90}-x_{10}}{x_{50}}$	S_V m²/cm³	$\varepsilon_{C,ML}$ %
Source mat.	SM	1.44	12.90	28.63	39.62	2.11	1.36	50
Fraction 1	F1	0.84	1.53	2.82	4.01	1.29	4.31	45
Fraction 2	F2	3.96	5.86	8.65	10.43	0.80	1.06	45
Fraction 3	F3	10.34	17.45	30.89	69.68	1.18	0.38	59

ChemElectroChem

Articles
doi.org/10.1002/celc.202001249

Chemistry Europe
European Chemical
Societies Publishing
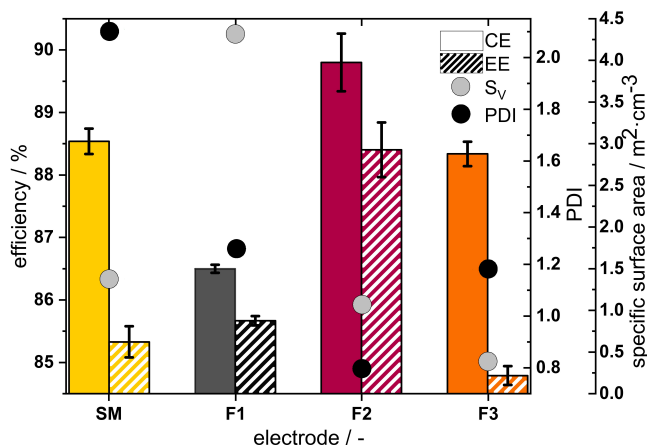
Figure 4. Coulombic (full) and energy (dashed) efficiencies of full cells and their standard deviation of the first formation cycle (C/10) compared to the specific surface area (grey dots) and the polydispersity index (black dots) for all four electrode types.

Figure 5. Nominal voltages of full cells during discharge (solid) and charge (dashed) for the different electrode types; second cycle C/10 at 25 °C.

$$CE = \frac{Q_{discharge}}{Q_{charge}} \cdot 100 \ \%$$

where E is the Energy and Q is the electric charge used during a full discharge or charge.

Among the electrodes with the various PSD, F2 shows the highest coulombic efficiency from the charge/discharge cycle during the first formation step, whereas F1 has low coulombic efficiency, i.e. it was not able to release a significant part of the stored lithium capacity during discharge. This results in a higher loss in retrieved electrons (contributed to the side reaction, for example, reduction of the electrolyte) as compared to the previously stored electrons into batteries. Theoretically, F3 should deliver the best coulombic efficiency, given that the side reactions are only dependent on the specific surface area. A possible explanation for the lower coulombic efficiency in F3 compared to F2 is that the overpotential difference between the charge and discharge steps that arose in F3 causes the abort criterion to be met sooner. Another possible explanation is that the current density is too high for the small specific surface area in coarser particles that causes other SEI reaction. Compared to coulombic efficiency, energy efficiency yields a different electrode ranking. Again, the narrow PSD of medium-size particles (F2) turns out to offer the best energy efficiency among all, but it is now followed by the smallest particles F1, source material and the coarsest particles F3. The negligible overpotential of F1, visible in Figure 3, is the most likely cause of why F1 shows a better energy efficiency than F3.

In order to better understand the electrode potential effects from the different particles without the impact from the SEI growth and aging effects, we look at the second C/10-cycle shown in Figure 5. The nominal voltage was hereby calculated using the arithmetical mean of the charge/discharge curve in the whole potential window.

The voltage loss can be well correlated with the particle size: As particle size increases, a large lithium-ion concentration gradient within the particle is developed due to the longer diffusion pathway, resulting in a higher overpotential inside the battery. Indeed, the difference of the average potential increases from the small particle size (F1) to the medium (F2) to the coarse (F3). The difference is especially pronounced for F3, confirming that stronger impact of overpotential in these electrodes. The potential drop from source material is about 102 mV, which is between F2 and F3 but closer to F3. Although F2 and source material exhibited almost similar S_V, the voltage drop of source material was about two times higher than F2. This is because the broader PSD of source material includes a greater fraction from coarser particles relative to smaller ones. Thus, the massive potential drop in source material needs to be attributed to the coarse particles. Therefore, it is essential to consider not only the surface area but also the particle size and PSD for optimizing energy efficiency.
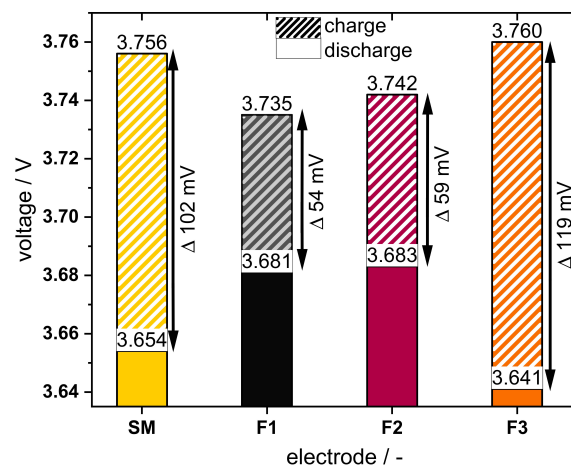
We now look on the phase after formation and the first C-rate test and investigate charging at 1C (7th cycle) and first long term aging effects (29th cycle). The goal is to find out the aging behavior for different particle size and PSD. Figure 6 shows the potential of the negative electrode during charging for the 7th cycle and 29th cycle at 1C charging.

It can be seen that F1 and F2 show nearly the same progression of the potential during 1C charging between 7th and 29th cycle. While their negative electrode potentials are always above zero volt, the potential of F3 and source material significantly drop below zero volt, which is known to trigger lithium plating. As discussed before, we attribute these high overpotential to the longer diffusion pathways in coarse particles. For both F3 and source material, the relatively steep potential drop below zero volt is followed by a slow increase in potential, which is assigned to lithium plating. All curves show a potential drop during CC operation followed by a slight increase during CV operation. With increasing cycle number, the potential below zero volt from F3 and source material appear later during the charge cycle, so that lithium plating occurs at higher charge capacity. Also the potential progression changes strongly during the cycling. It can be seen that an increase in particle size x_{50} with nearly same PDI (F1 to F3) leads

ChemElectroChem

Articles
doi.org/10.1002/celc.202001249

Chemistry Europe
European Chemical
Societies Publishing
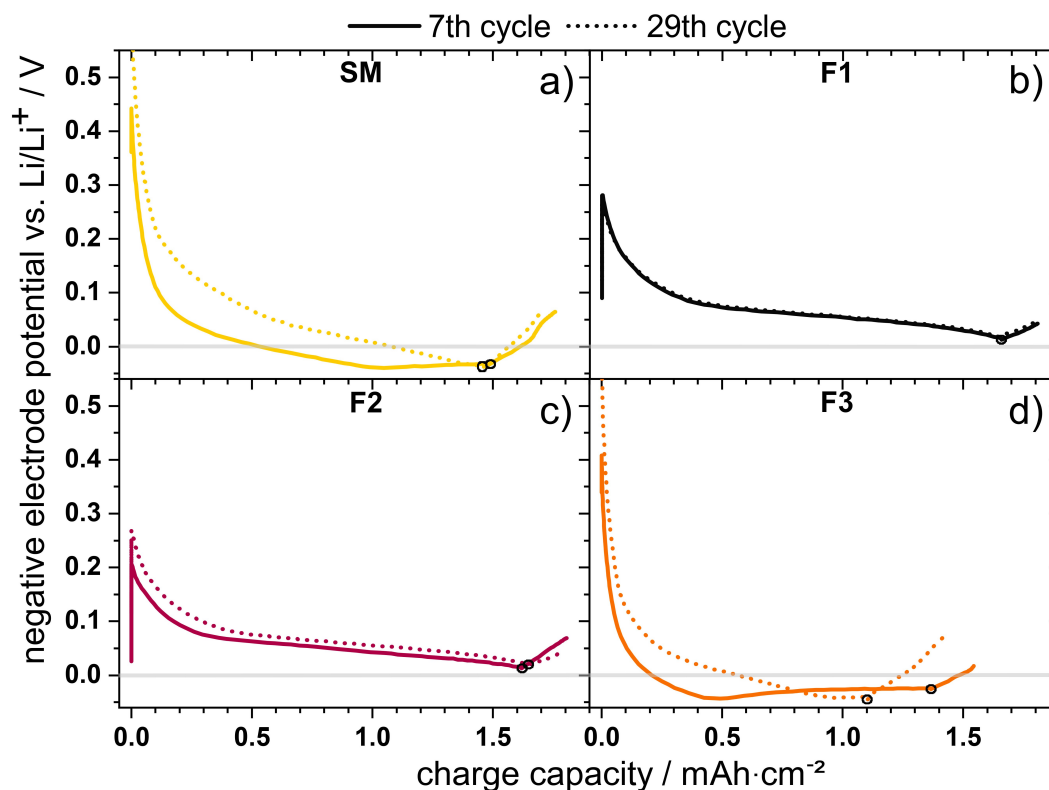
Figure 6. Negative electrode potential of a lithium/graphite half cell for the investigated electrode types during charging for 7th cycle (solid) and 29th cycle (dotted) for source material (a), F1 (b), F2 (c), and F3 (d); circle: change from CC to CV step; vertical line at the beginning of charging: IR-drop.

to higher capacity in the CV step compared to the CC step. In contrast, F1 and F2 show almost identical behavior to the fresh cell and also no negative voltage is detected.

Buqa et al.[25] reported that the particle size and electrode thickness are the deciding factors in avoiding lithium plating and poor rate capability. Based on our findings, we suggest that a higher amount of coarse particles in a broad distribution, which also corresponds to less surface area, increases the risk of lithium plating, particle cracking and contact loss as well as causes a longer charging time frame due to an earlier CV step.

Figure 7 shows the microscopic scan after the cycling test from F2 (left) and F3 (right). It is shown that in comparison with the surface before assembling, as shown in Figure 11 (first from the right), an obvious deposition on the surface of F3 after cycling can be seen. After cell opening, the deposition on the

surface of F3 looks metallic. This metallic deposition was removable with isopropanol. Upon washing, gas bubbles can be seen, which could be hydrogen gas as the reaction product of the metallic lithium with a protic solvent. Therfore, we identified this deposition mainly as plated lithium. Against that, as shown in Figure 7 no change of the surface can be seen and thus, no lithium plating can be detected for F2. This is also in accordance with our previous findings (Figure 6).

C-rate Test

Batteries need to be operated also at higher currents. To evaluate the effect of particle size and PSD on operation at higher current, a C-rate capability test was conducted.

In Figure 8, the potential of full cells during discharge is shown for different C-rates for the fresh cells and after 51 cycles. As expected, higher capacities can be achieved for lower C-rates due to less kinetic losses. The previous discussion on higher kinetic losses for coarser particles is also confirmed here: F1 and F2 provide the best C-rate capability as compared to F3 and source material. The voltage loss of up to 20 mAh/g can be seen for coarser particles, especially for source material and F3, which supports the prior conclusion of higher kinetic losses happen with the coarse particles. For low C-rates in F3 and source material, a change in curve progression at about 25 mAh/g of discharge is also noticeable. Such behavior is

Figure 7. Negative electrode surface of F2 and F3 electrodes after cycling; surface deposition indicates lithium plating.

ChemElectroChem

Articles
doi.org/10.1002/celc.202001249

Chemistry Europe
European Chemical
Societies Publishing
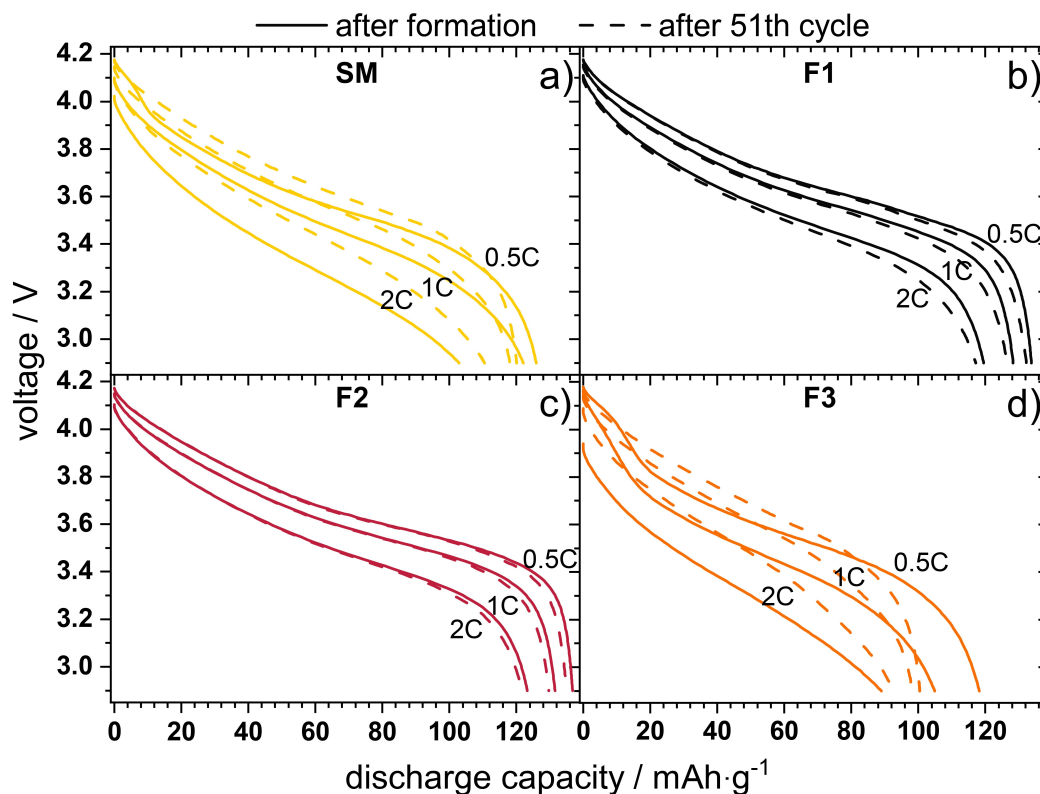
Figure 8. Full cell voltage vs. discharge capacity for all PSD-electrodes; C-rate test after formation (solid) and after 51 cycles (dashed) for source material (a), F1 (b), F2 (c), and F3 (d).

known to occur for stripping of plated Li as reported by Smart et al.,[55] and correlates with the finding of the negative electrode potential being under zero volt (see Figure 6). Again, we strongly suggest that lithium plating occurs earlier in broader PSD with coarser particles.

Notable differences in the C-rate behavior can also be seen due to cell aging. After 51 cycles, F1 and F2 showed nearly unchanged discharge curves with only slightly higher overall overpotential due to the SEI growth and minimal decrease in discharge capacity compared to after formation. Meanwhile, F3 and source material show strong differences. After cycling, the curve progression appears to be smoother without showing a strong decline at the beginning of discharge, whereby reversible lithium plating and stripping are no longer taking place. Further, all potentials are significantly higher than before cycling with high C-rates showing the best improvement in voltage and thus, in kinetic losses. An explanation for lower kinetic losses is that the C-rate test was conducted with an aging-adjusted lower current. As capacity loss was stronger in F3 and source material, current was reduced more significantly (up to 30%) for those electrodes, resulting in higher impact on the discharge curve and less kinetic losses. Overall, we can conclude that the rate capability improves as the particle size x_{50} decreases. But, for broad particle size distribution (source material), the rate capability is dominated by the coarser particles.

Electrochemical Impedance Spectroscopy

In order to separately determine and analyse the impact of particle size and PSD on ohmic losses, kinetic losses and mass transport losses and to see the effect of aging on these, electrochemical impedance spectra were measured. Figure 9 shows the Nyquist plot of the measured impedances. Note that selected frequencies are marked to study the processes and losses at their characteristic frequencies.

The recorded EIS spectra can be divided into four domains: the high frequency x-intercept contains resistance from current collector, measurement cables, and electric as well as ionic resistance through electrode and electrolytes (>1 kHz). A small semicircle is visible in the high frequency region (1 kHz to 100 kHz) and one semicircle at medium frequencies (100 Hz to 0.2 Hz). Finally, there is a straight line at low frequencies (< 0.2 Hz). The high frequency semicircle is often assigned to the transport through and at the SEI, as electrochemical reactions at both electrodes are usually slower. These in combination with double layer capacitance charging are expected to cause the subsequent semicircle. The straight line at the end of the low frequency region can be associated with slow transport processes, especially lithium solid diffusion within the active material.[56–59]

In Figure 9, it can be seen that there is a significant difference between the impedances of electrodes with different fractions and the source material. The impedance magnitude |Z| at frequency

ChemElectroChem

Articles
doi.org/10.1002/celc.202001249

**Chemistry
Europe**
European Chemical
Societies Publishing
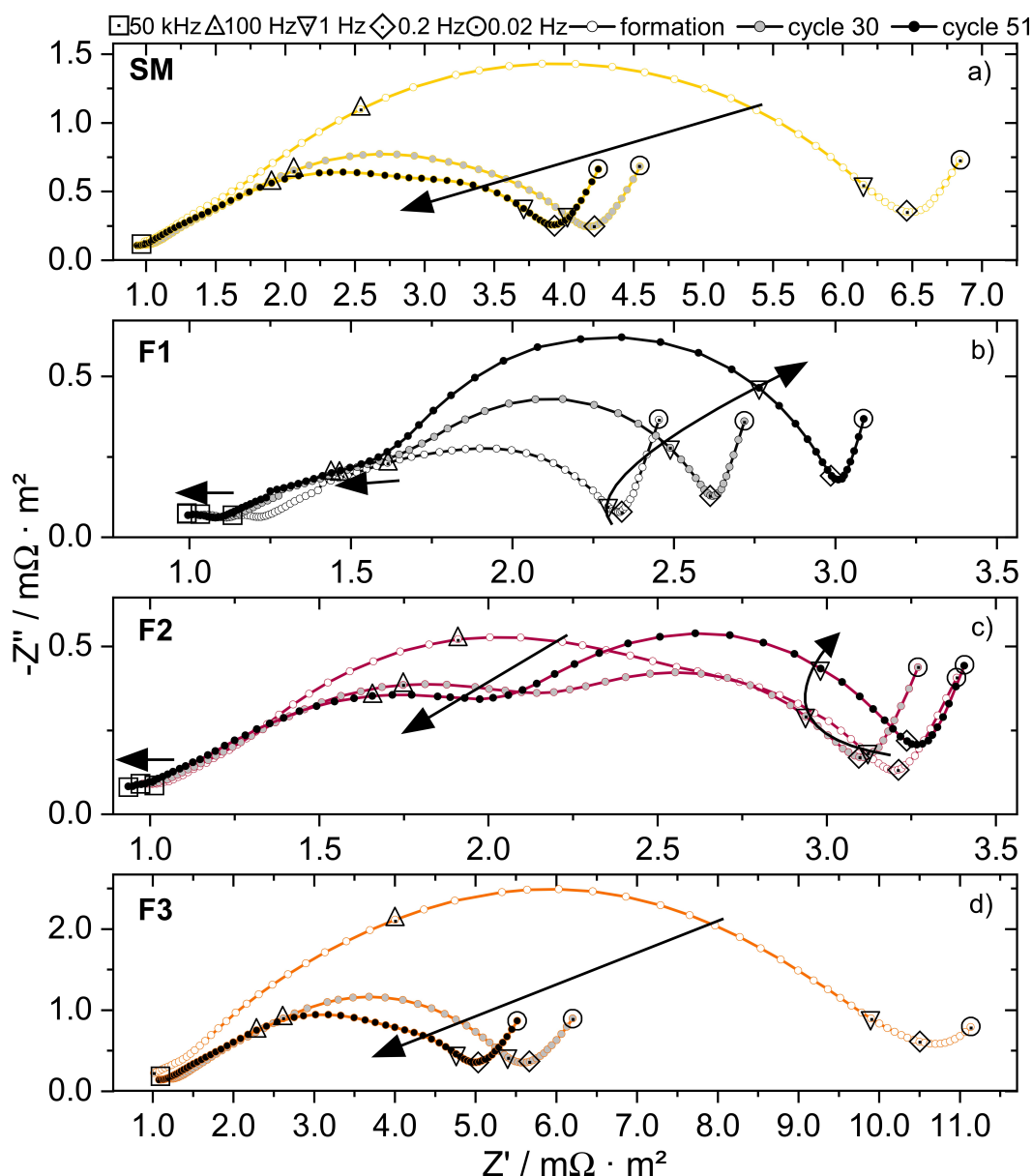
Figure 9. EIS measurements of lithium-ion full cells at 25 °C and SOC 50 % after formation, cycle 30 and cycle 51 for source material (a), F1 (b), F2 (c), and F3 (d); the arrow indicates the progression of the curves with time; for better visualisation, the axis were scaled differently for source material to F3.

0.02 Hz, which contains the cumulative contribution of SEI and kinetic and transport losses, are in accordance with the results from the galvanostatic charge/discharge experiments: F1 and F2 show the overall lowest impedances and the best C-rate capability and capacity, whereas source material and F3 reveal high impedances and poor C-rate capability and capacity, respectively. Generally, impedance increases with mean particle size, where F1 after formation shows about 2.4 mΩm² at 0.02 Hz, followed by F2 with 3.4 mΩm² and F3 with 11 mΩm² at last. In the high and middle frequency region (1 kHz to 0.2 Hz), we observe for F1 and F2 two seperated semicircles. This is in contrast to F3 and source material, where these two semicircles are combined together. Thus, the SEI effect is more dominant in F1 and F2 as compared to the kinetic losses due to charge transfer. In F3 and source material,

the kinetic losses are more dominant than the SEI effect. Comparing source material to the other particles, we see a similar trend as in the previously discussed rate capability and negative electrode overpotentials: Despite source material having much smaller average particle size than F3, source material and F3 behave very similar. This implies that particle size distribution is more important not only for rate capability and overpotential but also in EIS. Up to 50 kHz, the x-intercept is not yet visible possibly due to interface effects such as the contact resistance between grain boundaries, particles, and current collectors.[60] This interpretation is supported by the fact, that contrary to normal negative electrodes we do not use any conducting additives in the negative electrode, and thus, expect worse contact resistances.

ChemElectroChem

Articles
doi.org/10.1002/celc.202001249

Chemistry Europe
European Chemical
Societies Publishing

The impedance spectra at different aging times allow us to identify changing contributions especially of SEI, reaction and resistance. For F1 and F2, we see an increase of the low frequency semicircle and the characteristic time constant, suggesting more kinetic losses. In contrast, the kinetic contributions in F3 as well as in source material suggest an improvement in kinetics. Possible explanations for the latter phenomenon have been suggested by Bieker et al..[61] The impedance decrease is explained as the compaction of the material during aging or the micro-/macrocracking of the coarser particles that causes higher surface or the lithium plating/stripping process, that is also shown in Figure 2. During aging, the SEI effect in F1 and F2 improved, but the kinetic losses increase over cycles. Although the kinetic losses decrease drastically due to cycling for F3 and source material, the semicircle in the higher frequency region is not visible. The fractions without coarse particle size, F1 and F2, show that impedances in the high frequency region decrease, which could possibly be due to the improvement of particle contact or of SEI properties, e.g. via morphological changes that lead to a more compact and ionic conductive layer.

Source material and F2 have almost similar specific surface area and differ in terms of distribution width, but the impedance from source material is higher than F2. This is because the broad distribution of source material consists of a greater fraction of coarse particles like F3 and a tiny fraction of small particles like F1 and F2. Hence, it is seen that both PSD and particle size have a particular influence on the impedance behavior. The coarser and broader the PSD is, the greater the impedance corresponds to the kinetic losses.

Conclusions

Active material particles in electrodes naturally come with a different distribution of particle sizes, which is mainly caused by their production process. This work presented an experimental study on the impact of particle size and particle size distribution from negative graphitic electrode materials on cell performance and degradation of lithium-ion batteries. General trends for performance and cycling stability with respect to the particle size and particle size distribution could be identified and should be taken into consideration when selecting or tailoring active material for electrodes.

Our experimental investigations revealed that there is a non-monotonous correlation between particle size and capacity. At very small particles as in F1 (x_{50} of about 1.5 µm), the SEI losses lead to lower capacities, while above that, there is a clear trend in increasing capacity with decreasing x_{50} particle size. In contrast, particle size distribution has a more apparent effect on overpotentials and kinetic behavior. Here, the performance seems to be especially dominated by the coarse particles. For example, cells with source material, which has a broad distribution and contains thus coarser particles from fraction F3, shows electrochemical behavior which resembles that of F3. Despite the mean source material particle size is between F2 and F3. It can be concluded that both particle size

and particle size distribution impact performance of lithium-ion batteries.

Besides performance, we also investigated the degradation behavior of the cells. Here, many effects predicted by previous simulation results[20,36,40,62] can be confirmed in this experimental study: Very small particle sizes lead to high capacity loss mainly due to strong SEI growth whereas coarse particles are prone to lithium plating. A broader PSD is experienced to lead to faster degradation of cycling behavior, and thus, significantly reduces the performance of cells, because it contains the aging effects from both small and coarse particles: The small particle size causes strong SEI growth during formation and the coarse particle size results in high kinetic and capacity loss as well as lithium plating. Furthermore, a notable impedance decrease in the coarser particles or broad PSD are found to occur during aging whereas the large kinetic and transport losses lead to in general much larger overall impedance and overpotential. Here, two processes are suggested to occur during aging of electrodes with coarse particles: Microcracking may cause a larger surface area and may lead to more capacity loss but lower kinetic overpotentials. On the other hand, reversible lithium plating may be reduced during aging.

In conclusion, we recommend using medium particle size with narrow PSD to improve battery performance, longer life time, and safety. Furthermore, our results lay a solid basis for a model-based optimal design of electrodes, that will help to reduce experimental-only tailoring efforts, which are tedious, slow, and costly. Thus, it allows for a faster economic battery design. We recommend that not only the particle size but also the PSD must be considered for experimental or model-based optimization.

Experimental Section

Active Material Tailoring and Physical Characterisation

The active material used for electrode manufacture in this study was an artificial graphite mesocarbon microbeads powder (MCMB, OSAKA) with a specific capacity of 325 mAh/g. It was separated into three different fractions (F1, F2 and F3) with different particle size using a single wheel air classifier (CFS 5 HD-S, NETZSCH-CONDUX MAHLTECHNIK GMBH). The different PSD were obtained by varying the speed of the classifying wheel, process air flow rate and the mass loading of process air. The graphite powders that were employed for electrode manufacture were characterized using laser diffraction measurements (Helos, H1873, Cuvette R2, SYMPATEC GMBH) for determining the PSD and the calculated S_V. Figure 10 depicts the volumetric distribution density (q3) function of the three fractions F1 to F3 and the source material (SM).

Table 1 shows the measured and computed characteristic parameters for the individual materials, such as S_V and PDI, which describe the distribution width of a particle mixture. The PSD of the investigated source material ranges from 0.4 µm to 60 µm. From the source material, three fractions were separated as mentioned above. F1 shows the smallest mean particle size (x_{50}) and the highest S_V, F2 features nearly two times higher x_{50} and a similar S_V as the source material, and F3 has the coarsest particle size and the lowest S_V. It is visible that the three fractions and the source

ChemElectroChem

Articles
doi.org/10.1002/celc.202001249

Chemistry Europe
European Chemical
Societies Publishing
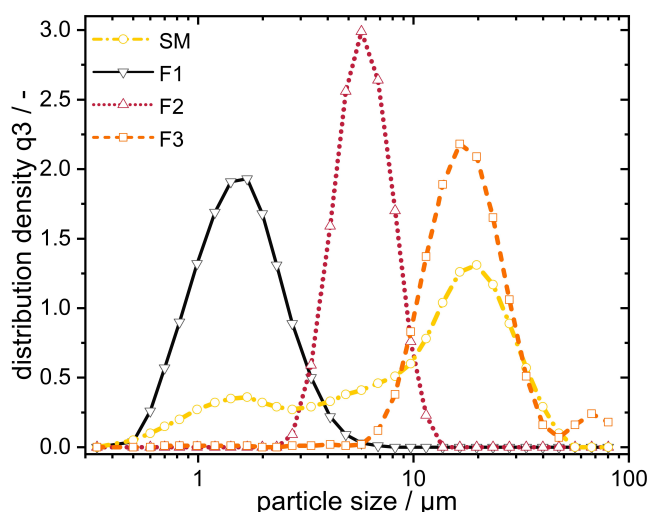
Figure 10. Distribution density q3 (volume) of the particle size for source material (SM) and the three fractions F1 to F3.

material show significant deviations in S_V, particle size and PSD among each other.

Every fraction shows a significant deviation from the source material in terms of these characteristic parameters. In comparison to the source material, the PDI of the individual fractions are about two times smaller. F2 and source material show an approximately similar S_V. This enables one to distinguish between the impact of S_V and PDI.

Electrode Production

The obtained material fractions as well as the source material were used to prepare four different electrodes with defined active material PSD, respectively. The preparation of the negative electrode was similarly described in literature.[63] All four electrodes contain 96 wt.% of classified or source active material, 2 wt.% of styrene butadien rubber (SBR, Lipaton SB 5521, SYNTHOMER) as binder and 2 wt.% of sodiumcarboxymethyl cellulose (Na-CMC Walocel Na-CMC2000 PA, DOW WOLFF CELLULOSICS GMBH) as suspension stabilizer accordingly. The dry electrode components (MCMB and Na-CMC) were dry mixed for 15 min in a rotary drum mixer (Turbula® T2F, WILLY A. BACHOFEN CORP.) with a rotational speed of 49 min⁻¹. The obtained powder mixture was then dispersed in deionized water in a three step process using a dissolver (Dispermat CA, VMA GETZMANN GMBH) with a 50 mm toothed disk. In the first step, the premixed powders were dispersed for 60 min. Next, SBR was added into the suspension after having been evacuated under vacuum for 10 min. Finally, the slurry

was coated on a 10 µm copper foil via a continuous pilot plant scale coater (Labco, KR-NERT GMBH & Co. KG) with a comma bar reverse roll application system. The drying process was performed in a three-stage convective drying process (DRYTEC GMBH & Co. KG) at a temperature of 65 °C. The coating and drying speed was set to 2 m/min. The resulting mass loading for all negative electrodes is 8.7 ± 1.2 mg/cm² and the measured electrode thicknesses (Digimetic Indicator, 543–575, MITUTOYO GMBH; sampling number n = 21) were 74 ± 4 µm for source material, 78 ± 5 µm for F1, 69 ± 4 µm for F2 and 66 ± 5 µm for F3. The electrodes were examined regarding their porosity based on the coating mass loading of each electrode by mercury intrusion porosimetry (Quantachrome, Poremaster 60 GT) and are listed in Table 1. The used method for porosimetry is described by Froböse and Titscher et al..[18] The porosity was calculated two times in between 30 nm and the x_{98} of the PSD of the active material. For the source material, therefore, the upper limit was set to the same value as for F3. The lower boundary was chosen with the awareness, that no conductive additives was used in these electrodes and therefore no smaller pores are expected.

Positive electrodes have been produced by CUSTOMCELLS ITZEHOE GMBH. They contain about 14 wt.% of additives including binder and conductive additive and an active material content of 86 wt.% of a nickel manganese cobalt oxide with the ratio of the different transition metals of 1:1:1 (NMC111). They feature a specific capacity of 145 mAh/g and an area specific capacity of 2.0 mAh/cm².

Microscopic analysis

Electrodes of all fractions (F1 to F3) and the source material were scanned under a laser scanning microscope (VK-9710, KEYENCE DEUTSCHLAND GMBH; Nikon, 150X/0.95, W.D. = 0.2) before assembly to visualize the electrode surface with different particle size and PSD. In Figure 11, the surfaces of the electrodes before assembly are shown. For post mortem analysis, the negative electrode surface was washed twice with DMC to remove the rest of the electrolyte and was then examined microscopically to detect lithium plating.

Cell Assembly

In order to investigate the influence of the PSD on performance, for all electrochemical experiments a commercial three-electrode setup from EL-CELL GMBH was used. This setup was used with circular electrodes with a diameter of maximum 18 mm and a separator with an embedded lithium reference ring electrode. As for separator, a polypropylen (PP)/polyethylene (PE) separator with a thickness of 220 µm and a porosity of 67% for PP and 86% for PE (EL-CELL GMBH; ECC1-00-0210 V/X) was used. The electrodes were punched with a diameter of 18 mm, weighed and heated overnight at 120 °C under high vacuum before being transferred into the
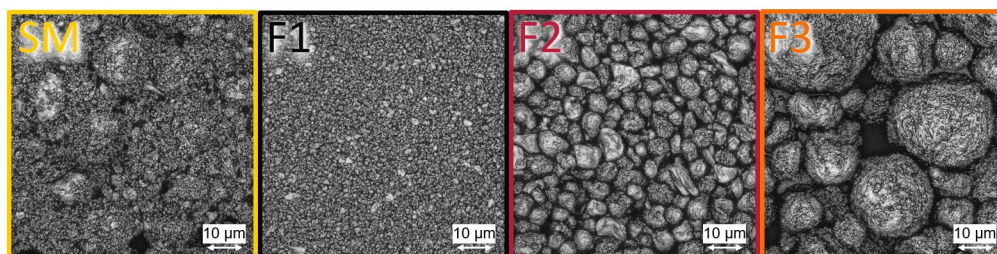
Figure 11. Microscopy images of electrode surface for source material (SM) and F1 to F3.

ChemElectroChem

Articles
doi.org/10.1002/celc.202001249

Chemistry Europe
European Chemical
Societies Publishing

argon glovebox (water and oxygen content under 0.1 ppm). All capacities of the electrodes were calculated based on the measured weight (scales XS205, Mettler Toledo) of the assembled electrodes. The cells were filled with 103 μL of electrolyte, which consists of ethylene carbonate (EC) and dimethyl carbonate (DMC) with a ratio of 1:1 (v/v) and 1 M LiPF$_6$ (Sigma-Aldrich, battery grade). Four measurements for each fraction F1 to F3 and source material were conducted.

Electrochemical Characterization

All three-electrode cells were cycled with a Maccor potentiostat (Maccor Inc., Series 4000) in a temperature chamber (Espec Europe GmbH, SU 642) at 25 °C in the voltage range between 2.9 V and 4.2 V. All potentials given are vs. Li/Li$^+$ as reference electrode. The formation and cycling procedure was identical for all experiments and is given in Table 2.

The cell formation process was carried out by using 2 cycles of C/10 in a CC step (constant current) and 1 cycle of C/10 with a CC/CV step (constant current/constant voltage). The CV step was stopped at currents equal to or less than C/20. The determined capacity from the CC/CV step was used to set the charge/discharge current of the respective C-rate (only the first C-rate test and first 1C cycling). The formation was followed by a discharge C-rate test, whereby the cells were two times discharged with C/2, 1C and 2C in a CC step and charged with 1C in a CC/CV step. The cells were then cycled at 1C, where charging was performed with CC/CV and discharging with CC. Finally, a second 1C cycling and C-rate test was carried out (via redetermined charge/discharge current of the respective C-rate).

EIS measurement were performed three times (EIS protocol listed in Table 3): Once after formation and two times during cycling. A Gamry 3000 potentiostat with auxiliary electrometer (Gamry) was used for this investigation, and the impedances were measured at a state of charge (SOC) of 50 % with the galvanostatic mode and an amplitude of $5 \cdot 10^{-4}$ A$_{rms}$ between the frequencies of 10^{-2} Hz to 10^6 Hz. The SOC 50 % was set as follows: The penultimate discharge step before the EIS measurements was conducted by CC/CV and the capacity to set the current of the C-rate was redetermined. Then, the cell was discharged with C/10 for 5 h. After each EIS measurement, the charge/discharge current was changed to the respective C-rate, for example, the 1C cycling of the new capacity.

Table 2. Cycling procedure.

Parameter	Value
Temperature	25 °C
Formation	C/10
C-rate test	2x [0.5;1;2]C
Cycle	1C
Charge	CC/CV
Discharge	CC
U$_{(cut-off)}$	4.2 V / 2.9 V

Table 3. Parameters of EIS.

Parameter	Value
Temperature	25 °C
Mode	galvanostatic
AC current	$5 \cdot 10^{-4}$ A$_{rms}$
Frequency	10^{-2} Hz to 10^6 Hz
Points/decade	10

[1] V. Agubra, J. Fergus, *Materials* **2013**, *6*, 1310–1325.
[2] F. Joho, B. Rykart, A. Blome, P. Novák, H. Wilhelm, M. E. Spahr, *J. Power Sources* **2001**, *97–98*, 78–82.
[3] T. D. Tran, J. H. Feikert, R. W. Pekala, K. Kinoshita, *J. Appl. Electrochem.* **1996**, *26*.
[4] H. F. Andersen, C. E. L. Foss, J. Voje, R. Tronstad, T. Mokkelbost, P. E. Vullum, A. Ulvestad, M. Kirkengen, J. P. Mæhlen, *Sci. Rep.* **2019**, *9*, 14814.
[5] M. Gauthier, D. Mazouzi, D. Reyter, B. Lestriez, P. Moreau, D. Guyomard, L. Roue, *Energy Environ. Sci.* **2013**, *6*, 2145.
[6] S.-C. Hou, Y.-F. Su, C.-C. Chang, C.-W. Hu, T.-Y. Chen, S.-M. Yang, J.-L. Huang, *J. Power Sources* **2017**, *349*, 111–120.
[7] M. Nöske, S. Breitung-Faes, A. Kwade, *Silicon* **2019**, *11*, 3001–3010.
[8] T. Pan, J. Alvarado, J. Zhu, Y. Yue, H. L. Xin, D. Nordlund, F. Lin, M. M. Doeff, *J. Electrochem. Soc.* **2019**, *166*, A1964-A1971.
[9] A. D. Jara, A. Betemariam, G. Woldetinsae, J. Y. Kim, *Int. J. Min. Sci. Technol.* **2019**, *29*, 671–689.
[10] H. Wang, T. Ikeda, K. Fukuda, M. Yoshio, *J. Power Sources* **1999**, *83*, 141–147.
[11] H. Zheng, M.-S. Kim, *Carbon Lett.* **2011**, *12*, 243–248.
[12] H. Bockholt, M. Indrikova, A. Netz, F. Golks, A. Kwade, *J. Power Sources* **2016**, *325*, 140–151.
[13] W. Haselrieder, S. Ivanov, D. K. Christen, H. Bockholt, A. Kwade, *ECS Trans.* **2013**, *50*, 59–70.
[14] A. Kwade, W. Haselrieder, R. Leithoff, A. Modlinger, F. Dietrich, K. Droeder, *Nat. Energy* **2018**, *3*, 290–300.
[15] V. Laue, O. Schmidt, H. Dreger, X. Xie, F. Röder, R. Schenkendorf, A. Kwade, U. Krewer, *Energy Technol.* **2020**, *8*, 1900201.
[16] C. Meyer, H. Bockholt, W. Haselrieder, A. Kwade, *J. Mater. Process. Technol.* **2017**, *249*, 172–178.
[17] J. Smekens, R. Gopalakrishnan, N. Steen, N. Omar, O. Hegazy, A. Hubin, J. van Mierlo, *Energies* **2016**, *9*, 104.
[18] L. Froboese, P. Titscher, B. Westphal, W. Haselrieder, A. Kwade, *Mater. Charact.* **2017**, *133*, 102–111.
[19] V. Laue, N. Wolff, F. Röder, U. Krewer, *Energy Technol.* **2020**, *8*, 1801049.
[20] F. Röder, S. Sonntag, D. Schröder, U. Krewer, *Energy Technol.* **2016**, *4*, 1588–1597.
[21] M. Petzl, M. A. Danzer, *J. Power Sources* **2014**, *254*, 80–87.
[22] Q. Liu, C. Du, B. Shen, P. Zuo, X. Cheng, Y. Ma, G. Yin, Y. Gao, *RSC Adv.* **2016**, *6*, 88683–88700.
[23] B. Epding, A. Broda, B. Rumberg, H. Jahnke, A. Kwade, *J. Electrochem. Soc.* **2019**, *166*, A1550-A1557.
[24] N. Harting, N. Wolff, U. Krewer, *Electrochim. Acta* **2018**, *281*, 378–385.
[25] H. Buqa, D. Goers, M. Holzapfel, M. E. Spahr, P. Novák, *J. Electrochem. Soc.* **2005**, *152*, A474.
[26] C. Wang, A. J. Appleby, F. E. Little, *J. Electroanal. Chem.* **2001**, *497*, 33–46.
[27] H. Buqa, A. Würsig, D. Goers, L. J. Hardwick, M. Holzapfel, P. Novák, F. Krumeich, M. E. Spahr, *J. Power Sources* **2005**, *146*, 134–141.
[28] D. Goers, M. E. Spahr, A. Leone, W. Märkle, P. Novák, *Electrochim. Acta* **2011**, *56*, 3799–3808.
[29] M. E. Spahr, D. Goers, W. Märkle, J. Dentzer, A. Würsig, H. Buqa, C. Vix-Guterl, P. Novák, *Electrochim. Acta* **2010**, *55*, 8928–8937.
[30] T. G. Zavalis, M. Klett, M. H. Kjell, M. Behm, R. W. Lindström, G. Lindbergh, *Electrochim. Acta* **2013**, *110*, 335–348.

ChemElectroChem

Articles
doi.org/10.1002/celc.202001249

Chemistry Europe
European Chemical
Societies Publishing

[31] J. Vetter, P. Novák, M. R. Wagner, C. Veit, K. C. Möller, J. O. Besenhard, M. Winter, M. Wohlfahrt-Mehrens, C. Vogler, A. Hammouche, *J. Power Sources* **2005**, *147*, 269–281.

[32] T. Drezen, N.-H. Kwon, P. Bowen, I. Teerlinck, M. Isono, I. Exnar, *J. Power Sources* **2007**, *174*, 949–953.

[33] G. T.-K. Fey, Y. G. Chen, H.-M. Kao, *J. Power Sources* **2009**, *189*, 169–178.

[34] W.-R. Liu, Z.-Z. Guo, W.-S. Young, D.-T. Shieh, H.-C. Wu, M.-H. Yang, N.-L. Wu, *J. Power Sources* **2005**, *140*, 139–144.

[35] W. Mei, H. Chen, J. Sun, Q. Wang, *Sustainable Energy Fuels* **2019**, *3*, 148–165.

[36] W. Du, A. Gupta, X. Zhang, A. M. Sastry, W. Shyy, *Int. J. Heat Mass Transfer* **2010**, *53*, 3552–3561.

[37] M. Farkhondeh, C. Delacourt, *J. Electrochem. Soc.* **2011**, *159*, A177-A192.

[38] D.-W. Chung, P. R. Shearing, N. P. Brandon, S. J. Harris, R. E. García, *J. Electrochem. Soc.* **2014**, *161*, A422-A430.

[39] K. Lee, D. Kum, in **2016** IEEE Transportation Electrification Conference and Expo, Asia-Pacific (ITEC Asia-Pacific), 454–459.

[40] S. T. Taleghani, B. Marcos, K. Zaghib, G. Lantagne, *J. Electrochem. Soc.* **2017**, *164*, E3179-E3189.

[41] M. Ender, J. Joos, A. Weber, E. Ivers-Tiffée, *J. Power Sources* **2014**, *269*, 912–919.

[42] C. Nowak, L. Froboese, M. Winter, T. Placke, W. Haselrieder, A. Kwade, *Energy Technol.* **2019**, *7*, 1900528.

[43] I. Capone, K. Hurlbutt, A. J. Naylor, A. W. Xiao, M. Pasta, *Energy Fuels* **2019**, *33*, 4651–4658.

[44] L. Chen, Z. Chen, S. Liu, B. Gao, J. Wang, *J. Electrochem. Energy Convers. Storage* **2018**, *15*.

[45] H. Nara, K. Morita, D. Mukoyama, T. Yokoshima, T. Momma, T. Osaka, *Electrochim. Acta* **2017**, *241*, 323–330.

[46] Y. Liu, H. Liu, X. Zhao, L. Wang, G. Liang, *J. Wuhan Univ. Technol. Mater. Sci. Ed.* **2019**, *34*, 549–557.

[47] F. Röder, R. D. Braatz, U. Krewer, *J. Electrochem. Soc.* **2017**, *164*, E3335-E3344.

[48] K. Takahashi, V. Srinivasan, *J. Electrochem. Soc.* **2015**, *162*, A635-A645.

[49] J. Christensen, J. Newman, *J. Solid State Electrochem.* **2006**, *10*, 293–319.

[50] R. Deshpande, M. Verbrugge, Y.-T. Cheng, J. Wang, P. Liu, *J. Electrochem. Soc.* **2012**, *159*, A1730-A1738.

[51] N. Lin, Z. Jia, Z. Wang, H. Zhao, G. Ai, X. Song, Y. Bai, V. Battaglia, C. Sun, J. Qiao, K. Wu, G. Liu, *J. Power Sources* **2017**, *365*, 235–239.

[52] S. Bhattacharya, A. R. Riahi, A. T. Alpas, *J. Power Sources* **2011**, *196*, 8719–8727.

[53] S. J. An, J. Li, C. Daniel, D. Mohanty, S. Nagpure, D. L. Wood, *Carbon* **2016**, *105*, 52–76.

[54] M. Winter, J. O. Besenhard, M. E. Spahr, P. Novák, *Adv. Mater.* **1998**, *10*, 725–763.

[55] M. C. Smart, B. V. Ratnakumar, *J. Electrochem. Soc.* **2011**, *158*, A379.

[56] S. J. An, J. Li, C. Daniel, H. M. Meyer, S. E. Trask, B. J. Polzin, D. L. Wood, *ACS Appl. Mater. Interfaces* **2017**, *9*, 18799–18808.

[57] E. Cuervo-Reyes, C. P. Scheller, M. Held, U. Sennhauser, *J. Electrochem. Soc.* **2015**, *162*, A1585-A1591.

[58] T. Momma, M. Matsunaga, D. Mukoyama, T. Osaka, *J. Power Sources* **2012**, *216*, 304–307.

[59] D. Mukoyama, T. Momma, H. Nara, T. Osaka, *Chem. Lett.* **2012**, *41*, 444–446.

[60] M. Gaberscek, J. Moskon, B. Erjavec, R. Dominko, J. Jamnik, *Electrochem. Solid-State Lett.* **2008**, *11*, A170.

[61] G. Bieker, M. Winter, P. Bieker, *Phys. Chem. Chem. Phys.* **2015**, *17*, 8670–8679.

[62] R. Darling, J. Newman, *J. Electrochem. Soc.* **1997**, *144*, 4201–4208.

[63] C. Sangrós Giménez, B. Finke, C. Nowak, C. Schilde, A. Kwade, *Adv. Powder Technol.* **2018**, *29*, 2312–2321.